Performance Comparison of Field-oriented Control, Direct Torque Control, and Model-predictive Control for SynRMs

*Hazem Hadla** *and Fernando Santos*

(Polytechnic Institute of Viseu, Higher School of Technology and Management of Lamego, Lamego 5100-074, Portugal)

Abstract: Simulation studies of three synchronous reluctance motor (SynRM) control strategies are presented: field-oriented control (FOC), direct torque control (DTC), and finite-set model-predictive control (FS-MPC). FOC uses linear controllers and pulse-width modulation to control the fundamental components of the load voltages vectors. In contrast, DTC and FS-MPC are nonlinear strategies wherein the voltage vectors are directly generated in the absence of a modulator. Theoretical operating principles and control structures of these control strategies are presented. Moreover, a comparative analysis of the static and dynamic performance of the control strategies is conducted using Matlab/Simulink to identify their advantages and limitations. It is confirmed that each of the control strategies has merits and that all three of them satisfy the requirements of modern high-performance drives.

Keywords: Field-oriented control, direct torque control, model-predictive control, synchronous reluctance motor

1 Introduction

The well-designed synchronous reluctance motor (SynRM) has recently attracted the attention of the industrial and scientific communities because it has a lower cost, a higher density, and simpler control than the induction motor [1-5]. Furthermore, the SynRM is seen as a better alternative to permanent-magnet synchronous motors and induction motors for applications such as fans, washing machines, and electric vehicles [6]. Additionally, owing to the absence of the winding and magnet in the rotor, it exhibits a higher energy efficiency and field-weakening capability [7].

High performance, a fast transient response, and appropriate control flexibility of electric drives are essential requirements for various industrial applications [8]. Two control techniques that have been widely investigated and reported for SynRM drives are field-oriented control (FOC) and direct torque control (DTC) [9-12]. FOC is a linear strategy that uses linear controllers and a pulse-width modulator to generate the voltages to be applied to the motor. Because FOC exhibits good performance under both steady-state and transient operating conditions, it has been widely used in electric drive systems [13-14]. The control strategies for the SynRM drive based on FOC can be divided into three main categories: constant *d*-axis current control, current angle control (CAC), and active flux control. These categories mainly differ in the method of generating the reference value of the currents in the rotor reference frame [15-17]. Maximum torque per ampere control can be considered a type of CAC; the objective of this control strategy is to maximize the electromagnetic torque for a given motor supply current. This is equivalent to the minimization of the motor copper losses for each torque value, which results in a high efficiency of the drive system [18-19]. Despite FOC providing a good dynamic torque and flux response, its structure is complex owing to the use of proportional-integral (PI) controllers and a modulator block, and tuning is necessary to achieve good performance.

Compared with FOC, DTC has a simpler structure, as it does not have any axis-transformation or modulator blocks. In this control strategy, the optimal voltage vector is selected from a predefined switching

Manuscript received February 1, 2021; revised July 4, 2021; accepted August 2, 2021. Date of publication March 31, 2022; date of current version September 8, 2021.

* Corresponding Author, E-mail: hrhadla@gmail.com

Digital Object Identifier: 10.23919/CJEE.2022.000003

table according to the position of the stator-flux vector and error signals provided by torque and stator-flux hysteresis controllers [20]. Despite the fast dynamic response achieved by DTC, it suffers from performance degradation at low speeds, as well as a high torque and flux ripple. To reduce the torque and flux ripples of the standard DTC, space vector modulation (SVM) based DTC was applied to SynRM drives in Refs. [21-23]. However, although DTC-SVM is useful for attenuating the flux and torque ripples, it increases the complexity of the standard DTC [24]. In Ref. [25], a space vector pulse-width modulation-based DTC (SVPWM-DTC) was proposed to overcome the high torque ripples of the standard DTC. This approach significantly reduces the switching losses in the switches but leads to a large computational burden.

The FOC and DTC methods satisfy the requirements of most applications [26]. However, in recent years, model-predictive control (MPC) has been perceived as a favorable alternative to these control methods [27]. MPC offers several advantages, for instance, it has an intuitive design methodology, can incorporate constraints and nonlinearities in a straightforward manner, and has the ability of multivariable control. Therefore, it is considered a good choice in high-performance electric motor drives.

MPC is divided into two main categories: continuous-set MPC and finite-set MPC (FS-MPC) [28]. Continuous-set MPC requires a modulator, and its algorithm is complex [29]. In comparison, FS-MPC has attracted more research attention because of its easy implementation and constraint inclusion capabilities, e.g., overcurrent protection and switching-loss minimization [30-31].

FS-MPC does not require a modulator. The two main types of FS-MPC are torque predictive control and current predictive control (CPC) [32-33]. In FS-MPC, the inverter model is considered in the control structure. Each possible switching vector is considered in the calculation of the cost function. The one that yields the minimum value of the cost function is selected as the optimal output. FS-MPC has been successful in various applications in power electronics and electrical drive systems [34-37].

In this work, FOC, DTC, and finite-set current predictive control (FS-CPC) are discussed—starting from their theoretical concepts—to illustrate the different control concepts and system structures. The control strategies are evaluated in Matlab/Simulink to compare their performance under both transient and steady-state operating conditions. The remainder of this paper is organized as follows. Section 2 introduces the mathematical model of the SynRM. In Section 3, the theoretical principles of FOC, DTC, and MPC are presented. Section 4 presents the simulation results, and Section 5 presents the conclusions.

2 Mathematical model of SynRM

The voltage and flux equations of an SynRM in a *dq* rotor reference frame are as follows [38]

$$u_d = R_s i_d + \frac{\mathrm{d}\psi_d}{\mathrm{d}t} - \omega_r \psi_q \tag{1}$$

$$u_q = R_s i_q + \frac{\mathrm{d}\psi_q}{\mathrm{d}t} + \omega_r \psi_d \tag{2}$$

$$\psi_d = L_d i_d \tag{3}$$

$$\psi_q = L_q i_q \tag{4}$$

where u_d, u_q, i_d, i_q, ψ_d, and ψ_q represent the stator-voltage, current, and flux-linkage components, respectively; L_d and L_q represent the inductances of the stator windings along the *d*- and *q*-axes; R_s represents the stator winding resistance; and ω_r represents the rotor electrical angular speed.

The corresponding electromagnetic torque T_e and motor dynamic equation are as follows

$$T_e = \frac{3}{2} p(\psi_d i_q - \psi_q i_d) = \frac{3}{2} p(L_d - L_q) i_d i_q \tag{5}$$

$$T_e - T_L = J_m \frac{\mathrm{d}\omega_r}{\mathrm{d}t} + B_m \omega_r \tag{6}$$

where p, T_L, J_m, and B_m represent the number of pole pairs, the load torque, the moment of inertia of the rotor, and the viscous friction coefficient, respectively.

If both i_d and i_q are suitable selected values, the electromagnetic torque in Eqs. (5)-(6) can be controlled to satisfy the torque of the load and the speed command.

The electrical model of the SynRM is described above without consideration of the magnetic and cross-magnetic saturation effects. This phenomenon is

not considered in the present study. Thus, L_d and L_q are kept constant and set to their nominal values in the three control strategies.

3 Theoretical principles of control strategies

In this section, the theoretical principles of FOC, DTC, and MPC are discussed to illustrate the main concepts and control structures.

3.1 FOC strategy

The working principle of FOC is to decouple the stator currents into their flux- and torque-producing components (i_d and i_q, respectively). Consequently, this strategy guarantees separated control of the flux and torque of the machine [39-40].

Fig. 1 [41] displays the block diagram of a general vector control system for a SynRM drive. The FOC method employs three control loops.

The aim of the external control loop is to control the rotor speed and provides the reference torque T_e^*. The two internal control loops are aimed at regulating i_d and i_q to control the torque and flux of the motor. Both reference and measured stator-current components along the *d*- and *q*-axis feed the two current loops, which with the assistance of PI controllers, generate the reference voltages u_d^* and u_q^*. These voltages are then converted from the *dq* reference frame into a stationary reference frame and forwarded to the modulator, which produces the gate signals of the inverter power switches.

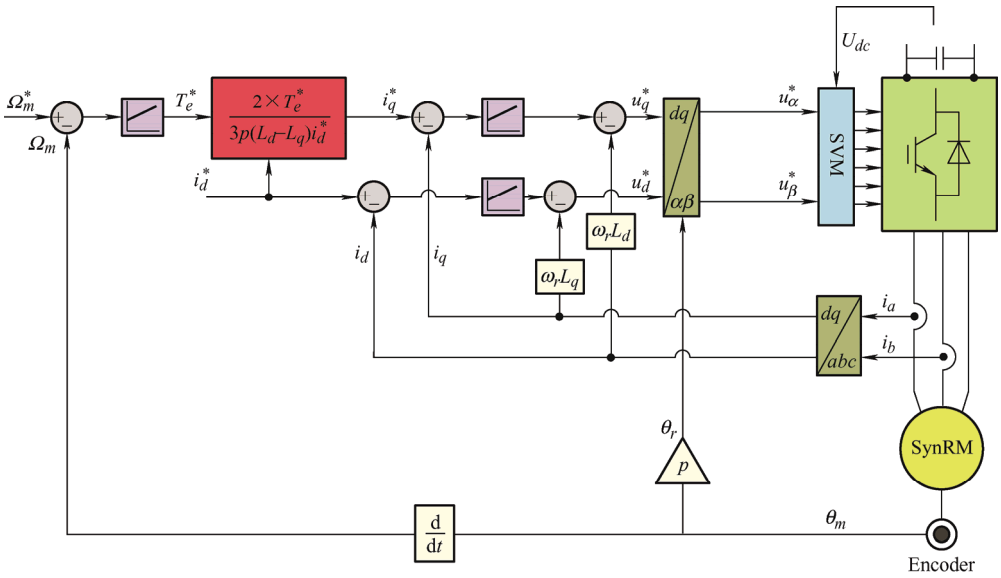

Fig. 1 Block diagram of a general FOC system for a SynRM drive

As shown in Fig. 1, the decoupling terms are employed in both current control loops to regulate i_d and i_q separately. The decoupling terms—$\omega_r\psi_d$ and $\omega_r\psi_q$—are calculated with the aid of the two voltage equations of the SynRM, i.e., Eqs. (1) and (2).

The transfer functions of the SynRM in the two current control loops (along the *d*- and *q*-axes) can be deduced through some mathematical manipulations, as follows

$$\begin{cases} G_d(t)=\dfrac{1}{sL_d+R_s}=\dfrac{1}{R_s(sT_{sd}+1)} \\ G_q(t)=\dfrac{1}{sL_q+R_s}=\dfrac{1}{R_s(sT_{sq}+1)} \end{cases} \tag{7}$$

where $T_{sd}=L_d/R_s$ and $T_{sq}=L_q/R_s$ are the electrical time constants along the *d*- and *q*-axes, respectively, and *s* is the Laplace variable.

The closed-loop system for current control is depicted in Fig. 2 [41].

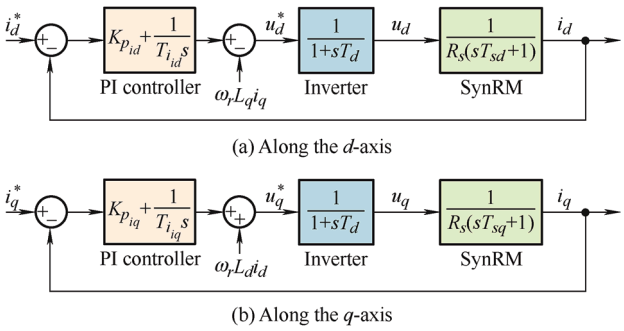

Fig. 2 Closed-loop system for current control

The inverter is commonly involved in the design

process of these closed-loop systems as a delay equal to [38]

$$T_d = \frac{T_s}{2} \tag{8}$$

where T_s represents the sampling time.

In the *s* plane, the delay caused by the inverter can be approximated by a first-order lag system [38]

$$u_{dq}(s) = \exp(-sT_s)u^*_{dq}(s) \approx \frac{1}{1+sT_d}u^*_{dq}(s) \tag{9}$$

The PI parameters of the current controllers are commonly designed using the amplitude method or the pole-placement method [42-43].

In spite of FOC providing a high dynamic torque and flux response, its structure is complex owing to the use of PI controllers and a modulator. Besides, it needs some tuning to accomplish good performance.

3.2 DTC strategy

Fig. 3 [41] displays the block diagram of a standard DTC scheme for SynRMs. It contains a stator-flux and torque observer, stator-flux and hysteresis controllers, and a switching table. In DTC, the torque and flux are regulated in a direct way, and there is no necessity for current control loops, in comparison to FOC. The stator-flux observer and torque estimator supply the estimated stator flux $\hat{\psi}_s$ and torque $\hat{T}_e$, respectively. The reference torque T_e^* is obtained using the speed controller, whereas the reference value of the stator-flux magnitude (ψ_s^*) is set to its nominal value. The working principle of DTC is to confine the torque error and flux error to small hysteresis bands by selecting suitable switching states of the hysteresis controllers (H_T), the stator-flux hysteresis controller (H_ψ), and the sector S_i in which the stator-flux vector is situated [44-45].

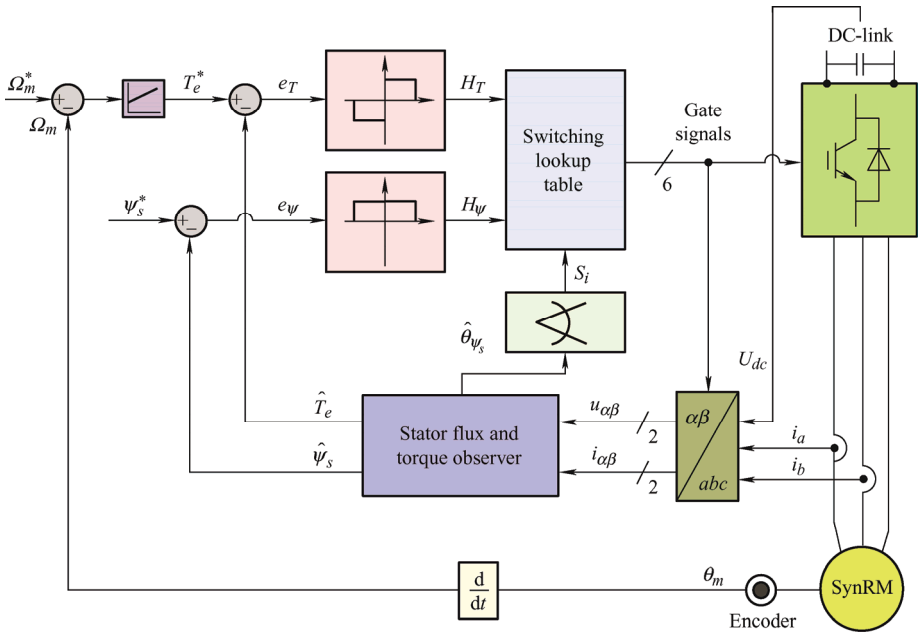

Fig. 3 Standard DTC scheme for SynRMs

In the implementation of the standard DTC, two hysteresis bands must be established: one for the torque and another for the stator-flux magnitude. For the torque, a three-level hysteresis controller is employed, whose outputs are as follows.

(1) 1: the torque must be increased.

(2) 0: the torque must be kept constant.

(3) –1: the torque must be reduced.

For the stator-flux magnitude, a two-level hysteresis controller is employed with two possible output values, as follows.

(1) 1: the stator-flux magnitude must be increased.

(2) 0: the stator-flux magnitude must be reduced.

A two-level classical voltage inverter can provide seven different voltage vectors, corresponding to the eight distinct switching states of the inverter. There are six voltage vectors of equal magnitude arranged 60° apart in the complex plane, as well as two zero vectors, as shown in Fig. 4 [41].

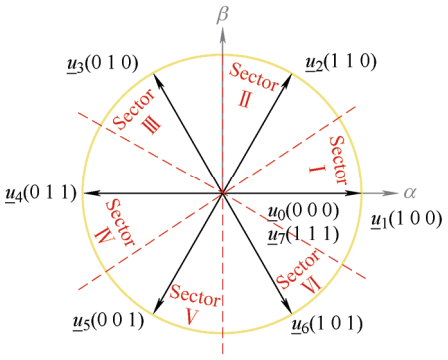

Fig. 4 Different voltage space vectors produced by the two-level voltage source inverter (2L-VSI)

The selection of the suitable voltage vector is relying on a functional block named "switching table" given by Tab. 1 [44] that provides binary signals applied to the inverter branches. The input quantities are the stator-flux sector and the outputs of the two hysteresis controllers, and the outputs are the voltage vectors.

Tab. 1 Switching table for standard DTC

H_ψ	H_T	Sector I	Sector II	Sector III	Sector IV	Sector V	Sector VI
	1	$\underline{u}_2$	$\underline{u}_3$	$\underline{u}_4$	$\underline{u}_5$	$\underline{u}_6$	$\underline{u}_1$
1	0	$\underline{u}_0$	$\underline{u}_7$	$\underline{u}_0$	$\underline{u}_7$	$\underline{u}_0$	$\underline{u}_7$
	–1	$\underline{u}_6$	$\underline{u}_1$	$\underline{u}_2$	$\underline{u}_3$	$\underline{u}_4$	$\underline{u}_5$
	1	$\underline{u}_3$	$\underline{u}_4$	$\underline{u}_5$	$\underline{u}_6$	$\underline{u}_1$	$\underline{u}_2$
–1	0	$\underline{u}_7$	$\underline{u}_0$	$\underline{u}_7$	$\underline{u}_0$	$\underline{u}_7$	$\underline{u}_0$
	–1	$\underline{u}_5$	$\underline{u}_6$	$\underline{u}_1$	$\underline{u}_2$	$\underline{u}_3$	$\underline{u}_4$

The stator flux of the motor in the stationary reference frame is estimated as follows

$$\begin{cases} \hat{\psi}_\alpha = \int (u_\alpha - R_s i_\alpha) \mathrm{d}t \\ \hat{\psi}_\beta = \int (u_\beta - R_s i_\beta) \mathrm{d}t \end{cases} \tag{10}$$

where $\hat{\psi}_\alpha$, $\hat{\psi}_\beta$, i_α, and i_β represent the $\alpha\beta$ components of the stator flux and the motor stator currents, respectively. The amplitude and angle of the stator-flux vector are given as follows

$$\begin{cases} \hat{\psi}_s = \sqrt{\psi_\alpha^2 + \psi_\beta^2} \\ \hat{\theta}_{\psi_s} = \arctan(\dfrac{\psi_\beta}{\psi_\alpha}) \end{cases} \tag{11}$$

In DTC, the electromagnetic torque in the stationary reference frame is estimated as follows

$$\hat{T}_e = \frac{3}{2} p(\psi_\alpha i_\beta - \psi_\beta i_\alpha) \tag{12}$$

In spite the rapid dynamic response attained by DTC, its performance degrades from a large torque and flux ripple, along with a variable switching frequency, in a traditional implementation. Furthermore, DTC is not resilient for the integration of control constraints.

3.3 MPC strategy

MPC is categorized into two main types: FS-MPC, which considers a finite set of switching actions, and continuous-set model-predictive control (CS-MPC), which needs a modulation phase to produce the switching actions. The FS-MPC technique is popular and attractive for power electronics and drive applications owing to its ease of execution and the exceptional dynamic performance given to the system under control. In this section, one of the well-known FS-MPC methods is presented. This strategy is called FS-CPC.

In FS-CPC, the voltage applied to the motor during each sampling interval belongs to the finite alphabet of actuations generated by the inverter. Therefore, in this study, the well-known 2L-VSI is selected and coupled to the SynRM, as shown in Fig. 5 [41]. The switching states of this converter are determined by the switching functions of the three legs: S_a, S_b, and S_c, which are defined as follows

$$S_i = \begin{cases} 1 & S_1 \text{ is on and } \overline{S}_1 \text{ is off} \\ 0 & S_1 \text{ is on and } \overline{S}_1 \text{ is on} \end{cases} \tag{13}$$

where $i \in \{a, b, c\}$.

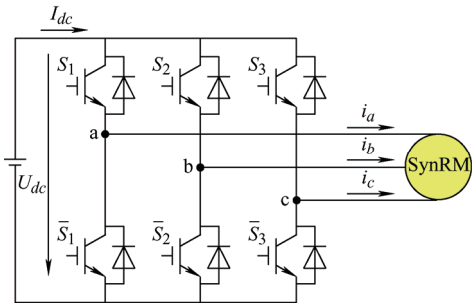

Fig. 5 2L-VSI feeding a SynRM

The inverter switching state can be expressed in the form of a complex vector

$$\underline{S} = \frac{2}{3}(S_a + \underline{a} S_b + \underline{a}^2 S_c) \tag{14}$$

where $\underline{a} = \exp(i 2\pi/3)$. The output voltage space vector generated by the 2L-VSI is given as

$$\underline{u}=\frac{2}{3}(u_a+\underline{a}u_b+\underline{a}^2u_c) \tag{15}$$

where u_a, u_b, and u_c represent the phase voltages at the motor terminals. The voltage vector $\underline{u}$ can be expressed in terms of the switching state $\underline{S}$ and the DC-link voltage U_{dc}

$$\underline{u}=U_{dc}\underline{S} \tag{16}$$

The inverter has a total of eight switching states. There are two identical zero voltage vectors $(\underline{u}_0=\underline{u}_7)$, resulting in only seven different voltage vectors. Therefore, in this study, a discrete system of the 2L-VSI with a total of seven different states as possible outputs is considered.

In this context, the inverter behaves as a discrete system. Therefore, the discrete voltage vectors presented in Tab. 2 are the only possible control actions for the SynRM drive.

Tab. 2 Voltage vectors of the 2L-VSI

u_n	$\boldsymbol{S}=[\boldsymbol{S}_a\ \boldsymbol{S}_b\ \boldsymbol{S}_c]$	$\underline{\boldsymbol{u}}=\boldsymbol{u}_\alpha+\boldsymbol{j}\boldsymbol{u}_\beta$
u_0	[0 0 0]	0
u_1	[1 0 0]	$2/3U_{dc}$
u_2	[1 1 0]	$1/3U_{dc}+j\sqrt{3}/3U_{dc}$
u_3	[0 1 0]	$-1/3U_{dc}+j\sqrt{3}/3U_{dc}$
u_4	[0 1 1]	$-2/3U_{dc}$
u_5	[0 0 1]	$-1/3U_{dc}-j\sqrt{3}/3U_{dc}$
u_6	[1 0 1]	$1/3U_{dc}-j\sqrt{3}/3U_{dc}$
u_7	[1 1 1]	0

3.3.1 Conventional FS-CPC of SynRM

A general diagram of the conventional FS-CPC for a SynRM is shown in Fig. 6. For designing the control strategy, Eqs. (1)-(4) are used to obtain the derivatives of the current with respect to time along the *d*- and *q*-axes, as follows

$$\begin{cases}\dfrac{\mathrm{d}i_d}{\mathrm{d}t}=\dfrac{u_d}{L_d}-\dfrac{R_s}{L_d}i_d+\dfrac{L_q}{L_d}\omega_r i_q\\[2ex]\dfrac{\mathrm{d}i_q}{\mathrm{d}t}=\dfrac{u_q}{L_q}-\dfrac{R_s}{L_q}i_q-\dfrac{L_d}{L_q}\omega_r i_d\end{cases} \tag{17}$$

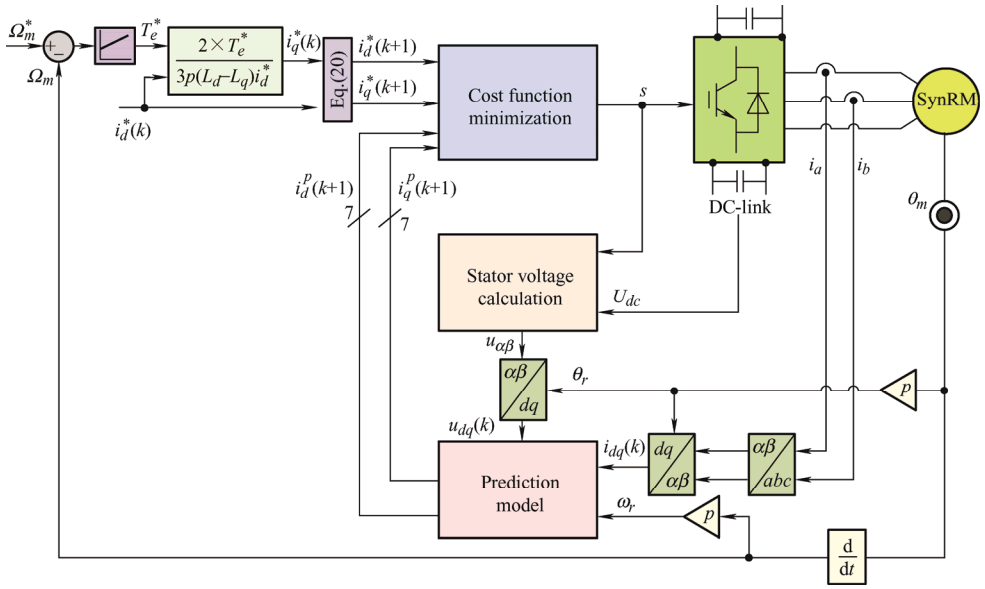

Fig. 6 Conventional FS-CPC of a SynRM

A discrete-time model is needed to predict the currents for the next sampling time. Thus, the forward Euler method is applied to the continuous-time model in Eq. (17) for a short sampling time T_s. Thus, the discrete-time model of the SynRM in the *dq* reference frame can be expressed as follows [46]

$$\begin{cases}i_d^p(k+1)=(1-T_s\dfrac{R_s}{L_d})i_d(k)+T_s\dfrac{L_q}{L_d}\omega_r i_q(k)+T_s\dfrac{u_d(k)}{L_d}\\[2ex]i_q^p(k+1)=(1-T_s\dfrac{R_s}{L_q})i_q(k)+T_s\dfrac{L_d}{L_q}\omega_r i_d(k)+T_s\dfrac{u_q(k)}{L_q}\end{cases} \tag{18}$$

where $i_d^p(k+1)$ and $i_q^p(k+1)$ represent the predicted currents at *k*+1, and $u_d(k)$ and $u_q(k)$ represent the voltage components at instant *k*, which are calculated with the knowledge of each of the eight switching states at instant *k* and the measured DC-link voltage U_{dc}.

The final step of the conventional FS-CPC strategy is the evaluation of the cost function for each of the seven different voltage vectors. The optimal voltage vector, i.e., the one that minimizes the cost function, is

selected to be applied to the motor at instant k. The cost-function formula is

$$g=\left|i_d^*(k+1)-i_d^p(k+1)\right|_{u_{0,\cdots,7}}\Big|+\left|i_q^*(k+1)-i_q^p(k+1)\right|_{u_{0,\cdots,7}}\Big|+C \tag{19}$$

Here, $i_{\max}$ represents the maximum allowable stator current of the SynRM, and $i_d^*(k+1)$ and $i_q^*(k+1)$ represent the reference stator currents in the dq reference frame, which can be computed using the previous reference currents $i_d^*(k)$ and $i_q^*(k)$ as follows [29]

$$\begin{cases} i_d^*(k+1)=3i_d^*(k)-3i_d^*(k-1)+i_d^*(k-2) \\ i_q^*(k+1)=3i_q^*(k)-3i_q^*(k-1)+i_q^*(k-2) \end{cases} \tag{20}$$

The term C in Eq. (19) represents the overcurrent protection to ensure that the safety current limits are respected. This term is given as

$$C=\begin{cases} 0 & \sqrt{i_d(k+1)^2+i_q(k+1)^2}\leqslant i_{\max} \\ \infty & \sqrt{i_d(k+1)^2+i_q(k+1)^2}>i_{\max} \end{cases} \tag{21}$$

The main disadvantage of conventional FS-CPC is a large computational burden, as seven predictions of the currents and seven evaluations of the cost function must be performed each sampling time. Thus, another control strategy called simplified FS-CPC is presented herein.

3.3.2 Simplified FS-CPC of SynRM

Fig. 7 shows the block diagram of simplified FS-CPC. In this control strategy, the reference voltage vector (RVV) is directly calculated from the reference currents. Using Eq. (18), the RVV can be computed by replacing the predicted currents at instant k+1 with the reference ones at the same instant [32-33]

$$\begin{cases} u_d^*(k)=R_s i_d(k)+L_d\dfrac{i_d^*(k+1)-i_d(k)}{T_s}-\omega_r L_q i_q(k) \\ u_q^*(k)=R_s i_q(k)+L_q\dfrac{i_q^*(k+1)-i_q(k)}{T_s}+\omega_r L_d i_d(k) \end{cases} \tag{22}$$

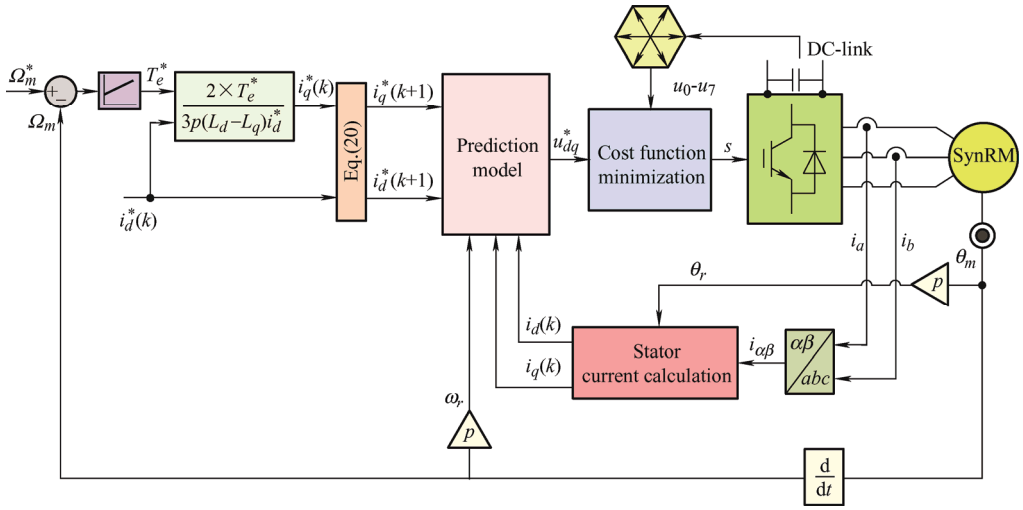

Fig. 7 Simplified FS-CPC of a SynRM

The final stage of simplified FS-CPC is the evaluation of a simple cost function for each of the seven different voltage vectors. This cost function represents the absolute value between the RVV and each of the voltage vectors that the inverter can apply to the motor.

$$g=\left|u_d^*(k)-u_{dn}\right|+\left|u_q^*(k)-u_{qn}\right| \quad n=0,1,\cdots,7 \tag{23}$$

In conclusion, simplified FS-CPC requires less computation time, because instead of seven predictions for the currents, the RVV is calculated only once, and a simple cost function is evaluated at the end. However, simplified FS-CPC operates with a variable switching frequency, which is considered to be its main limitation.

3.4 Comparison of different control strategies

In this section, the theoretical concepts and structures are compared. From the block diagrams of the control strategies shown above, one can conclude that all of them require speed PI control to achieve adjustable speed control. For the inner controllers, FOC uses two current PI controllers, DTC adopts two hysteresis controllers and a switching lookup table, and simplified FS-CPC uses a cost function to evaluate the voltage errors. Both FOC and simplified FS-CPC require a coordinate transformation. DTC is usually implemented in a stator reference frame; thus, no coordinate transformation is required. FOC needs a

modulator to handle the continuous variables, whereas the other control strategies do not require a modulator, owing to their direct control features. From the viewpoint of the tuning process, FOC has three PI controllers, for which six parameters must be calculated. DTC requires the calculation of four parameters for the PI controllers and two for the hysteresis system.

Simplified FS-CPC needs only two parameters for the external PI controller, and the cost function does not require a weighting factor.

In Tab. 3, these three control strategies are compared with regard to the number of tuned parameters, external and internal controllers, coordinate transformation, use of a modulator, inclusion of system constraints, and complexity.

Tab. 3 Comparison of the three control strategies

Features	FOC	DTC	Simplified FS-CPC
Number of tuned parameters	6	4	2
External controller	PI	PI	PI
Internal controller	2 PI	2 hysteresis	1 cost function
Coordinate transformation	Yes	No	Yes
Modulator	Yes	No	No
System constraint inclusion	Difficult	Difficult	Easy
Complexity	High	Medium	Low

4 Simulation results and discussion

The models of FOC, DTC, and simplified FS-CPC, which are shown in Figs. 1, 3, and 7, respectively, were simulated and validated using Matlab/Simulink. The nominal parameters of the studied SynRM are presented in Tab. 4 [41].

Tab. 4 Parameters of the SynRM

Parameter	Value
Rated power P/kW	3
DC-link voltage U_{dc}/V	650
Rated speed (mechanical) n_m/(r/min)	1 500
Rated current I_s/A	7.9
Nominal d-axis inductance L_d/H	0.186
Nominal q-axis inductance L_q/H	0.04
Nominal stator resistance R_s/Ω	1.35
Rated frequency f/Hz	50
Rotor inertia J/(kg • m^2)	0.079

For fair comparisons, the same sampling time (20 μs) was selected, and similar switching frequencies were reached at different operating points. As DTC and simplified FS-CPC have variable switching frequencies, the DTC value is taken as the reference. The hysteresis band of DTC is tuned through simulation. The PI controllers' values are obtained through the conventional trial-and-error-based empirical method with the principle of first-outer-then-inner controller tuning for FOC.

The first test was performed to examine the steady-state behavior. The motor was running at 700 r/min with a full load torque. Fig. 8 presents the results of the three control strategies, including the percentage of the torque ripple variation $\hat{e}_{(\text{torque ripple})}$ and the stator-current response. The control strategies exhibited good results. The calculated current total harmonic distortion (THD) was 0.174 3%, 0.32%, and 0.23% for FOC, DTC, and simplified FS-CPC, respectively. FOC reached the best current quality at the operating point; however, the other two control strategies also exhibited good results. To provide a general overview of the torque-ripple variation in the steady-state test, the torque ripple was calculated and is presented in Fig. 8 as a percentage of the peak error with respect to the average torque. As shown, FOC and simplified FS-CPC have smaller torque ripples than DTC (<3% and <4%, respectively). DTC has slightly larger torque ripples (>7.5%). According to the errors between the reference (19.1 N • m) and the average values of the torque ripples during the observation time, FOC has even better results. This is caused by the inner current PI controllers. FOC easily obtains good current waveforms owing to the independent PI control of the torque and the flux magnitude, as well as the use of a modulator. However, more parameters must be tuned for a cascaded PI control structure.

The average commutation frequency for the test presented in Fig. 8 was calculated, as shown in Fig. 9. The calculation is based on the mean value of the change in switching states over a period of 0.02 s, which is calculated from the present and past gate pulses. The mean value is divided by six (the number of active switches of the inverter) to obtain the switching frequency per insulated-gate bipolar

transistor (IGBT). The obtained values of the average commutation frequency for FOC, DTC, and simplified FS-CPC were 1.62 kHz, 1.66 kHz, and 1.67 kHz, respectively.

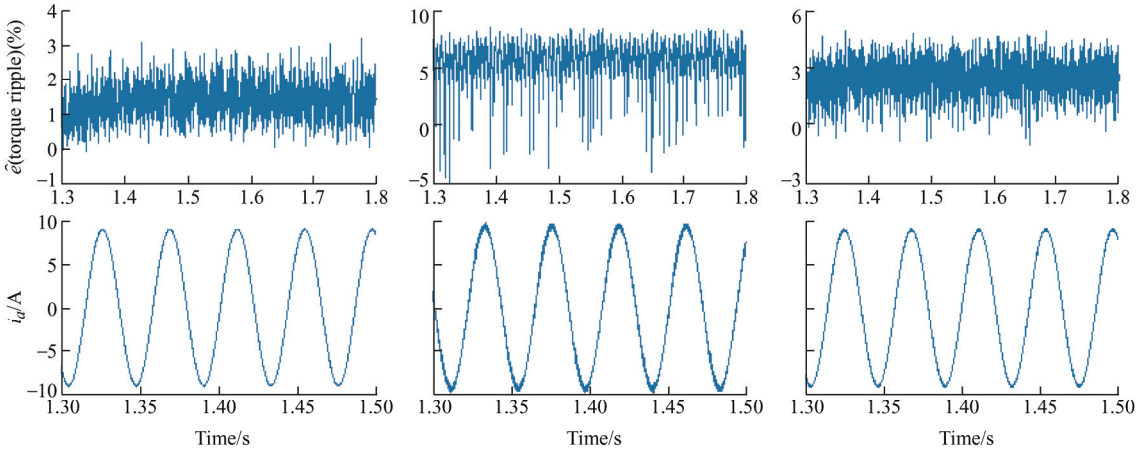

(a) FOC (b) DTC (c) Simplified FS-CPC

Fig. 8 Simulation results for the torque and stator-current behaviors of the three control strategies when the SynRM drive is running in the steady state at 700 r/min with a full load torque

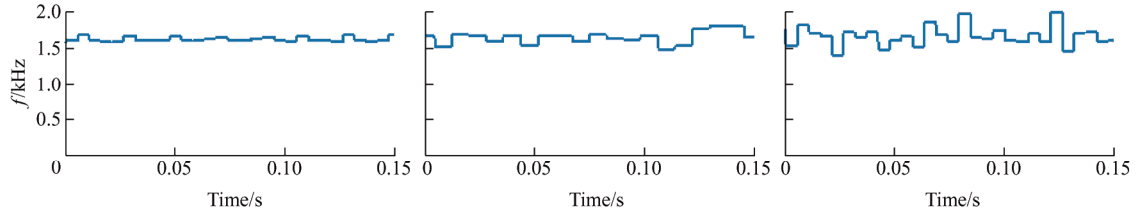

(a) FOC (b) DTC (c) Simplified FS-CPC

Fig. 9 Simulation results for the average commutation frequencies of the three control strategies for the operating point presented in Fig. 8

The dynamics of control strategies are fundamental to electrical drives. In the second test, the torque dynamics were compared. The torque reference changed from 0 N • m to the rated value at a speed of 700 r/min. Fig. 10 presents the test results. Clearly, the estimated torque $\hat{T}_e$ closely tracked its reference value T_e^*, and the three control strategies had fast dynamic responses, leading to the high performance of the SynRM drive. Moreover, during the test, the stator currents complied with the maximum current limitation (11.2 A) under the operating condition.

The results shown in Fig. 10 are supported by those shown in Fig. 11 (magnified view of the torque variations in the vicinity of t=0.1 s). According to these results, a variation from zero to the rated load torque was achieved in 4 ms, 2 ms, and 2 ms for FOC, DTC and simplified FS-CPC, respectively.

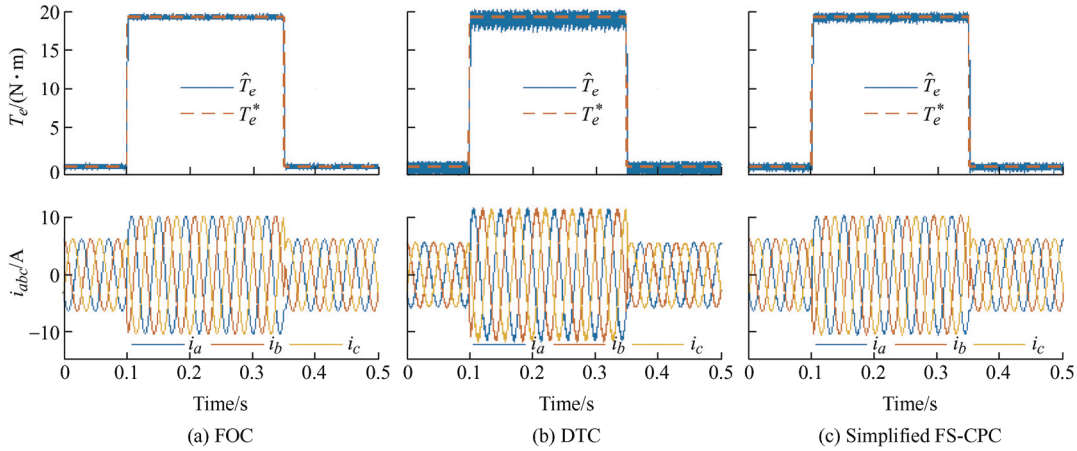

(a) FOC (b) DTC (c) Simplified FS-CPC

Fig. 10 Simulation results for the step torque responses of the three control strategies (torque command from 0 to 19.1 N • m) when the SynRM is running at 700 r/min

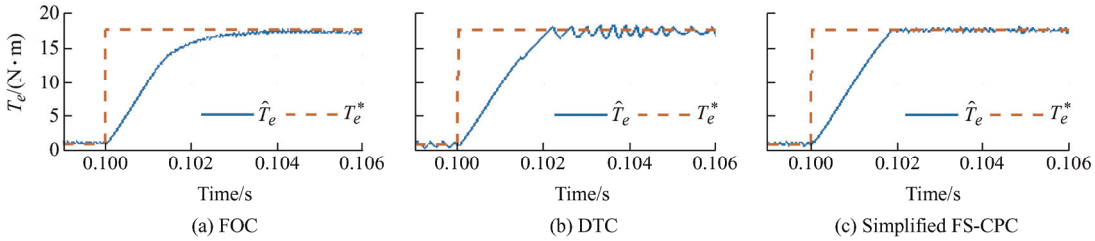

(a) FOC (b) DTC (c) Simplified FS-CPC

Fig. 11 Magnified views of the torque step responses in Fig. 10, showing the variations of the reference torque and actual motor torque in the vicinity of t=0.1 s

FOC needed a longer settling time (4 ms), but the two direct control strategies are faster (2 ms). The main reasons for the different settling time is that in the case of FOC, the inner current PI controller limits the bandwidth of the external speed PI controller, and it uses a modulator, which generates a delay. In contrast, the direct control strategies—DTC and simplified FS-CPC—theoretically have infinite bandwidths.

To compare the performance for a wider speed range, a speed-reversal test was conducted. This test was performed with the SynRM initially running at full speed (1 500 r/min) with a zero-load torque. Fig. 12 presents the results for the speeds, torques, and stator currents of the three control strategies. As shown, FOC, DTC, and simplified FS-CPC exhibited similar results; however, FOC achieved slightly better current results, owing to the use of the independent inner current PI controllers. Simplified FS-CPC also exhibited a good current waveform, because the error between the reference voltage and the measured voltage was evaluated in the cost function, making it easier for the tuning process to reach a good current response.

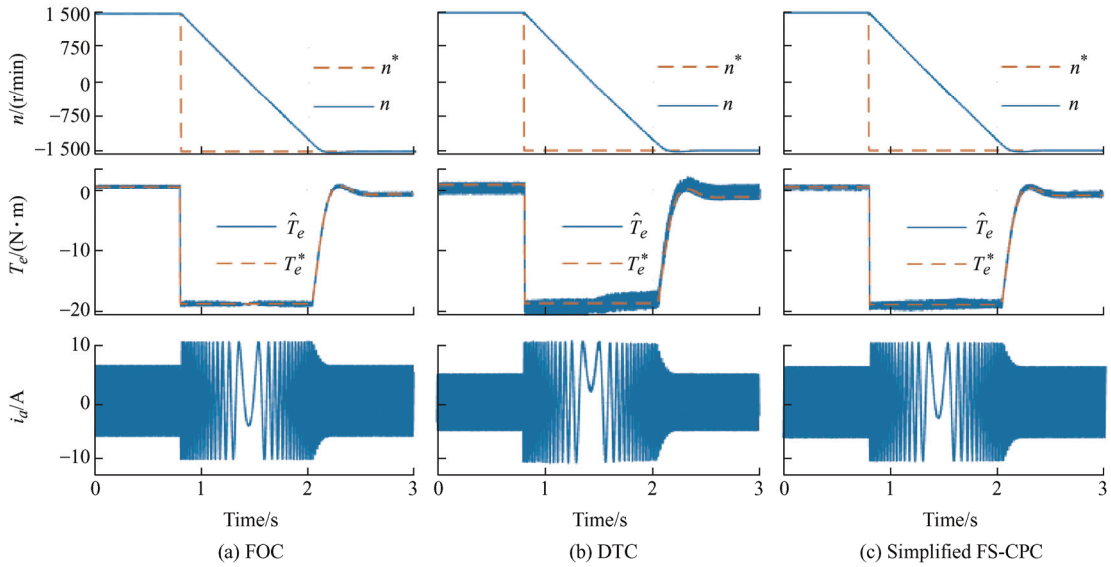

(a) FOC (b) DTC (c) Simplified FS-CPC

Fig. 12 Simulation results for the rotor speeds, torques, and current waveforms of the SynRM drive under the three control strategies during a speed reversal

Additionally, the measured speed had a smooth response and reached its desired value in a short time (approximately 1.4 s). The current limit was always satisfied, as the current i_a remained lower than the maximum allowed value (11.2 A).

A speed transition from 500 r/min to 1 200 r/min with a load torque of 10 N • m applied to the motor is depicted in Fig. 13. For the three control strategies, the speed tracked its reference value accurately without significant overshoot. Moreover, the speed rise times were comparable. During the acceleration period, the torque developed by the motor was the rated one, and after the desired speed was reached, a torque of 10 N •m was developed to satisfy the required load torque. The current limit was satisfied during the transient period.

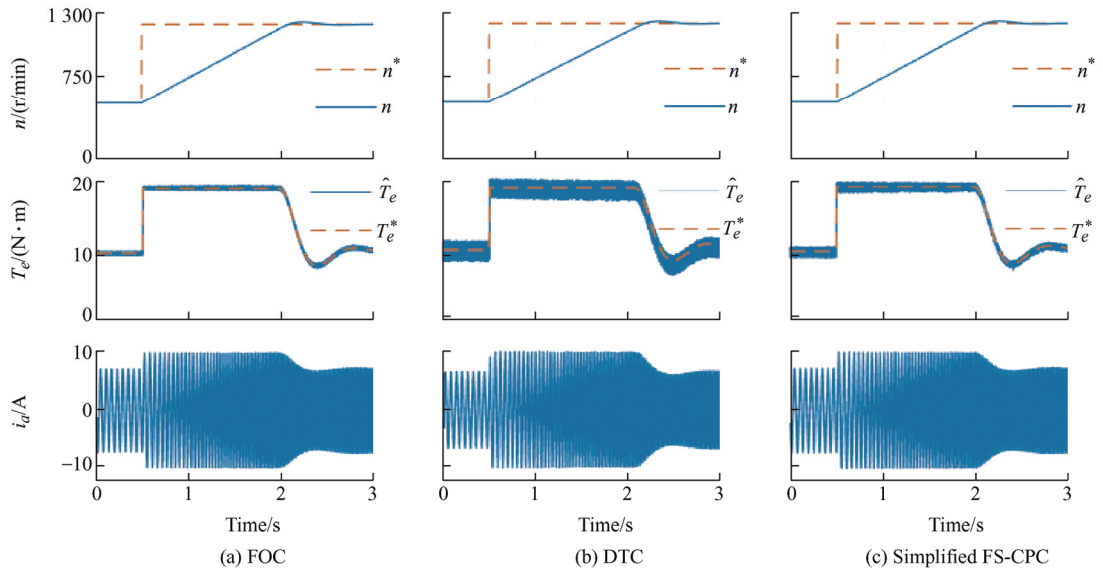

Fig. 13 Speed step responses of the three control strategies for a step speed command from 500 r/min to 1 200 r/min, with a load torque of 10 N • m

According to the simulation results, FOC, DTC, and simplified FS-CPC have good performance. Generally, FOC had a slightly better current THD and smaller torque ripples at almost all operating conditions. DTC and simplified FS-CPC have variable switching frequencies; however, they can be modified by adding SVM to achieve a better current THD. FOC has a longer settling time when the torque step test is performed. DTC has fast dynamics but large torque ripples, and simplified FS-CPC has good behavior, with small torque ripples and fast dynamics. The features of the three control strategies are compared in Tab. 5.

Tab. 5 Comparison of the three control strategies

Features	FOC	DTC	Simplified FS-CPC
Stator-current THD	Better	Worse	Good
Torque ripple	Less	More	Some
Torque response	Slower	Faster	Faster
Switching frequency	Constant	Variable	Variable

5 Conclusions

The theoretical principles and performance of three control strategies (FOC, DTC, and simplified FS-CPC) for the SynRM were compared. These strategies differ from a theoretical viewpoint. FOC exhibits a relatively slow torque response owing to the use of linear current controllers. The advantage of this control strategy is its constant switching frequency, which is determined by the presence of the modulator.

DTC, which appeared later in the market, is a direct nonlinear control strategy with a higher torque response. It operates with a variable switching frequency, which is considered as the drawback of this type of controller.

Both FOC and DTC are well established and have been recognized by the industrial and scientific communities as the preferred strategies for performance drives.

The simplified FS-CPC strategy was recently developed by the scientific community. It has a simple structure and operating principle. Using a cost function, in which various system constraints can be involved, the switching vectors are easily selected. Simplified FS-CPC exhibits a fast and good torque response; furthermore, it operates with a variable switching frequency, similar to DTC.

The simulation results indicated that all the control strategies had good performance in the whole speed range with or without a load torque applied to the motor. These control strategies generate currents of comparable quality under load conditions.

References

[1] R A Trubenbach, A T Mackay, M J Kamper. Performance of a reluctance synchronous machine under vector control. *Proceedings of IEEE Power Electronics Specialist*

Conference, 1993, Seattle, USA, PESC'93, 1993: 803-808.

[2] S M Taghavi, P A Pillay. Mechanically robust rotor with transverse laminations for a wide-speed-range synchronous reluctance traction motor. *Transactions on Industry Applications*, 2015, 51(6): 4404-4414.

[3] Z Li, X Bao. Analysis of vibration and noise of induction motor equipped with concentric single-double-layer star-delta winding. *Chinese Journal of Electrical Engineering*, 2019, 5(1): 36-46.

[4] M H V Reddy, K S Gowri, T B Reddy, et al. Effect of center voltage vectors (CVVs) of three-level space plane on the performance of dual inverter fed open end winding induction motor drive. *Chinese Journal of Electrical Engineering*, 2019, 5(2): 43-55.

[5] M Zhou, X Zhang, W Zhao, et al. Influence of magnet shape on the cogging torque of a surface-mounted permanent magnet motor. *Chinese Journal of Electrical Engineering*, 2019, 5(4): 40-50.

[6] A Farhan, M Abdelrahem, A Saleh, et al. Simplified sensorless current predictive control of synchronous reluctance motor using online parameter estimation. *Energies*, 2020, 13(2): 492-510.

[7] J Kolehmainen. Synchronous reluctance motor with form blocked rotor. *Transactions on Energy Conversion*, 2010, 25(2): 450-456.

[8] J W Finch, D Giaouris. Controlled ac electrical drives. *Transactions on Industrial Electronics*, 2008, 55(2): 481-491.

[9] A P Goncalves, S M A Cruz, F Ferreira, et al. Synchronous reluctance motor drive for electric vehicles including cross-magnetic saturation. *IEEE Vehicle Power and Propulsion Conference (VPPC)*, 2014, Coimbra, Portugal, VPPC'2014, 2014: 1-6.

[10] K Malekian, M R Sharif, J Milimonfared. An optimal current vector control for synchronous reluctance motors incorporating field weakening. *10th IEEE International Workshop on Advanced Motion Control*, 2008, Trento, Italy, AMC'08, 2008: 393-398.

[11] X Zang, G H B Foo. Over-modulation of constant switching frequency-based DTC for reluctance synchronous motors incorporating field-weakening operation. *Transactions on Industrial Electronics*, 2018, 66(1): 37-47.

[12] G H B Foo, X Zhang. Robust direct torque control of synchronous reluctance motor drives in the field-weakening region. *Transactions on Power Electronics*, 2017, 32(2): 1289-1298.

[13] R Antonello, L Ortombina, F Tinazzi, et al. Advanced current control of synchronous reluctance motors, *IEEE 12th International Conference on Power Electronics and Drive Systems (PEDS)*, 2017, Honolulu, USA, PEDS'2017, 2017: 1037-1042.

[14] P R Ghosh, A Das, G Bhuvaneswari. Performance comparison of different vector control approaches for a synchronous reluctance motor drive. *IEEE 6th International Conference on Computer Applications In Electrical Engineering-Recent Advances (CERA)*, 2017, Roorkee, India, CERA'2017, 2017: 320-325.

[15] T Lubin, H Razik, A Rezzoug, et al. Magnetic saturation effects on the control of a synchronous reluctance machine. *Transactions on Energy Conversion*, 2002, 17(3): 356-362.

[16] I Boldea, M C Paicu, G D Andreescu, et al. Active flux concept for motion-sensorless unified AC drives. *Transactions on Power Electronics*, 2008, 23(5): 2612-2618.

[17] J Pyrhönen, V Hrabovcová, R S Semken, et al. Electrical machine drives control: An introduction. New York: Wiley, 2016.

[18] L J Cheng, M C Tsai. Robust scalar control of synchronous reluctance motor with optimal efficiency by MTPA control. *IEEE Access*, 2021(9): 32599-32612.

[19] R Thike, P Pillay. Experimental investigation of MTPA trajectory of synchronous reluctance machine. *2018 IEEE International Conference on Power Electronics, Drives and Energy Systems (PEDES)*, Chennai, India, 2018.

[20] S Wiedemann, A Dziechciarz. Comparative evaluation of DTC strategies for the synchronous reluctance machine. *IEEE Tenth International Conference on Ecological Vehicles and Renewable Energies (EVER)*, 2015, Monte Carlo, Monaco, EVER'2015, 2015: 1-5.

[21] I Boldea, L Janosi, F Blaabjerg, et al. A modified direct torque control (DTC) of reluctance synchronous motor sensorless drive. *Electric Machines and Power Systems*, 2000, 28(2): 115-128.

[22] X Zhang, G H B Foo, M F Rahman, et al. A robust field-weakening approach for direct torque and flux controlled reluctance synchronous motors with extended constant power speed region. *Transactions on Industrial Electronics*, 2020, 67(3): 1813-1823.

[23] P R Ghosh, A Das, G Bhuvaneswari, et al. Comparative analysis of sensorless DTC schemes for a synchronous reluctance motor drive. *IEEE International Conference on Power Electronics, Drives and Energy Systems (PEDES)*, Chennai, India, 2018: 1-5.

[24] H Heidari, A Rassõlkin, A Kallaste, et al. A review of synchronous reluctance motor-drive advancements. *Sustainability*, 2021, 13(2): 729-766.

[25] C Che, Y Qu. Research on drive technology and control strategy of electric vehicle based on SVPWM-DTC. 2011 *International Conference on Mechatronic Science, Electric Engineering and Computer (MEC)*, Jilin, China, 2011: 44-49.

[26] M P Kazmierkowski, L G Franquelo, J Rodriguez, et al. High-performance motor drives. *Industrial Electronics Magazine*, 2011, 5(3): 6-26.

[27] P G Carlet, F Tinazzi, S Bolognani, et al. An effective model-free predictive current control for synchronous reluctance motor drives. *Transactions on Industry Applications*, 2019, 55(4): 3781-3790.

[28] P F C Gonçalves, S M A Cruz, A M S Mendes. Comparison of model predictive control strategies for six-phase permanent magnet synchronous machines. *44th Annual Conference of the IEEE Industrial Electronics Society*, 2018, Washington, DC, USA, IECO N'2018, 2018: 5801-5806.

[29] M Abdelrahem, C M Hackl, R Kennel, et al. Efficient direct-model predictive control with discrete-time integral action for PMSGS. *Transactions on Energy Conversion,* 2019, 34(2): 1063-1072.

[30] P Cortés, M P Kazmierkowski, R M Kennel, et al. Predictive control in power electronics and drives. *Transactions on Industrial Electronics,* 2008, 55(12): 4312-4324.

[31] J Rodriguez, R M Kennel, J R Espinoza, et al. High-performance control strategies for electrical drives: An experimental assessment. *Transactions on Industrial Electronics*, 2012, 59(2): 812-820.

[32] H Hadla, S Cruz. Active flux based finite control set model predictive control of synchronous reluctance motor drives. *18th European Conference on Power Electronics and Applications (EPE'16 ECCE Europe)*, 2016, Karlsruhe, Germany, EPE'2016, 2016: 1-10.

[33] H Hadla, S Cruz. Predictive stator flux and load angle control of synchronous reluctance motor drives operating in a wide speed range. *Transactions on Industrial Electronics*, 2017, 64(9): 6950-6959.

[34] F Wang, S Li, X Mei, et al. Model-based predictive direct control strategies for electrical drives: An experimental evaluation of PTC and PCC methods. *Transactions on Industrial Informatics*, 2015, 11(3): 671-681.

[35] R Kennel, J Rodriguez, J Espinoza, et al. High performance speed control methods for electrical machines: An assessment. *IEEE International Conference on Industrial Technology*, 2010, Vina del Mar, Chile, ICIT'2010, 2010: 1793-1799.

[36] J Rodriguez, M P Kazmierkowski, J R Espinoza, et al. State of the art of finite control set model predictive control in power electronics. *Transactions on Industrial Informatics*, 2013, 9(2): 1003-1016.

[37] Y Zhang, J Gao, C Qu. Relationship between two direct power control methods for PWM rectifiers under unbalanced network. *Transactions on Power Electronics*, 2017, 32(5): 4084-4094.

[38] C T Liu, P C Shih, S C Yen, et al. Theoretical and experimental investigations of the electromagnetic steel compositions for synchronous reluctance motors. *Transactions on Industry Applications*, 2018, 54(3): 2947-2954.

[39] D A Staton, T J E Miller, S E Wood. Maximising the saliency ratio of the synchronous reluctance motor. *IEE Proceedings B (Electric Power Applications)*, 1993, 140(4): 249-259.

[40] R E Betz, R Lagerquist, M Jovanovic, et al. Control of synchronous reluctance machines. *Transactions on Industry Applications*, 1993, 29(6): 1110-1122.

[41] H R Hadla. Predictive load angle and stator flux control of SynRM drives for the full speed range. Coimbra: Coimbra University, 2019.

[42] M Hinkkanen, H A A Awan, Z Qu, et al. Current control for synchronous motor drives: Direct discrete-time

pole-placement design. *Transactions on Industry Applications*, 2016, 52(2): 1530-1541.

[43] K H Ang, G Chong, Y Li, et al. PID control system analysis, design, and technology. *Transactions on Control Systems Technology*, 2005, 13(4): 559-576.

[44] T H Liu, H H Hsu. Adaptive controller design for a synchronous reluctance motor drive system with direct torque control. *The International Conference on "Computer as a Tool"*, 2007, Warsaw, Poland, EURCON'2007, 2007: 1725-1732.

[45] L Q Zhou. Direct torque control of ala synchronous reluctance machine based on modified integrator. *Power Conversion Conference - Nagoya*, 2007, Nagoya, Japan, PCCON'2007, 2007: 271-274.

[46] C K Lin, J T Yu, Y S Lai. Improved model-free predictive current control for synchronous reluctance motor drives. *Transactions on Industrial Electronics*, 2016, 63(6): 3942-3953.

Hazem Hadla was born in Homs, Syria, in 1982. He received a B.S. degree in Electrical Engineering from Al-baath University, Homs, Syria, in 2007, an M.S. degree in Electrical Machines from Cairo University, Cairo, Egypt, in 2013, and a Ph.D. degree in Electrical and Computer Engineering (electric drive systems specialty) from Coimbra University, Coimbra, Portugal, in 2018. His current research interests include electric drives and predictive control.

Fernando Santos was born in Coimbra, Portugal, in 1977. He received the B.S. degree in Electrical Engineering from Polytechnic Institute of Viseu, Viseu, Portugal, in 2001, and M.S. degree in Electrical and Computer Engineering (energy specialty) from Coimbra University, Coimbra, in 2003, and a Ph.D. degree in Electrical and Computer Engineering (energy systems specialty) from Coimbra University, Coimbra, Portugal, in 2016. His current research interests include nonlinear analysis and control of power supplies and AC drives.